



Originally published as:

Zhou, B., Liang, X., Lin, G., Tian, X., Zhu, G., Mechie, J., Teng, J. (2019): Upper Crustal Weak Zone in Central Tibet: An Implication From Three-Dimensional Seismic Velocity and Attenuation Tomography Results. - *Journal of Geophysical Research*, 124, 5, pp. 4654–4672.

DOI: <http://doi.org/10.1029/2018JB016653>

RESEARCH ARTICLE

10.1029/2018JB016653

Key Points:

- Seismic data from 53 temporary and 10 permanent stations are used to conduct velocity and attenuation tomography for central Tibet
- Shallow low- and high-Vp anomalies generally correspond to sedimentary basins and exhumed metamorphic blocks in the study area
- Upper crustal (or deeper) low-Vp zone along the Bangong-Nujiang suture reflects compositional difference along the ophiolitic mélange belt

Supporting Information:

- Supporting Information S1
- Table S1
- Table S2
- Table S3
- Table S4
- Table S5

Correspondence to:

X. Liang,
liangxf@mail.iggcas.ac.cn

Citation:





Zhou, B., Liang, X., Lin, G., Tian, X., Zhu, G., Mechie, J., & Teng, J. (2019). Upper crustal weak zone in central Tibet: An implication from three-dimensional seismic velocity and attenuation tomography results. *Journal of Geophysical Research: Solid Earth*, 124. <https://doi.org/10.1029/2018JB016653>

Received 3 SEP 2018

Accepted 1 APR 2019

Accepted article online 9 APR 2019

Upper Crustal Weak Zone in Central Tibet: An Implication From Three-Dimensional Seismic Velocity and Attenuation Tomography Results

Beibei Zhou^{1,2,3}, Xiaofeng Liang^{1,3} , Guoqing Lin⁴ , Xiaobo Tian^{1,5} , Gaohua Zhu⁶, James Mechie⁷ , and Jiwen Teng^{1,3}

¹State Key Laboratory of Lithospheric Evolution, Institute of Geology and Geophysics, Chinese Academy of Sciences, Beijing, China, ²College of Earth Sciences, University of Chinese Academy of Sciences, Beijing, China, ³Institutions of Earth Science, Chinese Academy of Sciences, Beijing, China, ⁴Department of Marine Geosciences, Rosenstiel School of Marine and Atmospheric Science, University of Miami, Miami, FL, USA, ⁵CAS Center for Excellence in Tibetan Plateau Earth Sciences, Beijing, China, ⁶Earth System Science Programme, Faculty of Science, Chinese University of Hong Kong, Hong Kong, China, ⁷Deutsches GeoForschungsZentrum - GFZ, Section "Geophysical Deep Sounding", Potsdam, Germany

Abstract A series of conjugate strike-slip faults is the most prominent geologic feature in central Tibet and is considered to accommodate east-west extension and coeval north-south contraction. The development mechanism of the conjugate strike-slip fault system is under debate because of unclear crustal physical properties and compositional variations. *P* and *S* wave arrivals from 414 local earthquakes recorded by the temporary Seismic Array Integrated Detection for a Window of Indian Continental Head array and the permanent China National Seismic Network were used for the velocity tomography, with additional *P* and *S* wave arrivals from 12 shots of the International Deep Profiling of Tibet and the Himalaya III reflection/refraction profile. The local earthquakes were simultaneously relocated with the updated velocity models. We also inverted for a three-dimensional upper crustal *Q_p* model with the same earthquake data set. The *V_p* structure near the surface shows that low-*V_p* anomalies generally correspond to sedimentary basins and high-*V_p* anomalies are related to exhumed metamorphic blocks in the study area. Relatively low *V_p*/*V_s* ratios in the upper crust indicate widely distributed quartz-rich rocks. The low-*V_p* zone from 0- to 10-km depth (resolving depth limit) is spatially correlated with the Bangong-Nujiang suture, possibly reflecting the compositional difference along the ophiolitic mélange belt accompanied by twin volcanic arcs from a double-sided subduction. This interpretation is supported by relatively heterogeneous *Q_p* values. This low-velocity zone also implies relatively uniform stress and continuous deformation in the upper crust of central Tibet. The relatively weak materials in at least the upper crust would result in strain concentration and help the development of the conjugate strike-slip fault system along the Bangong-Nujiang suture.

1. Introduction

The Himalaya-Tibetan orogen is one of the most active regions on the Earth (e.g., Yin & Harrison, 2000) and was formed by the collision and subsequent convergence between the Indian and Eurasian continents, roughly 65 Ma (e.g., Ding et al., 2005). The ongoing convergence is accompanied by north-south shortening and east-west extension (Langin et al., 2003; Liang et al., 2013; Molnar & Lyoncaent, 1989; Taylor & Peltzer, 2006). The north-south shortening began with continental collision and resulted in fold and thrust structures along the orogen (e.g., Li et al., 2015; Yin & Harrison, 2000). The east-west extension, which may have begun during the Miocene, is characterized by normal faults throughout Tibet and large-scale strike-slip faults along the boundaries of the plateau (e.g., Armijo et al., 1986, 1989; Molnar & Lyoncaent, 1989; Rothery & Drury, 1984; Royden et al., 2008). Interestingly, there is a V-shaped conjugate strike-slip fault system lying along the Bangong-Nujiang suture (BNS) zone in central Tibet (Figure 1). The conjugate strike-slip faults and associated north-south trending rifts are considered to accommodate coeval north-south shortening and east-west extension (Taylor et al., 2003).

Although there is widespread active faulting in Tibet to accommodate the convergence deformation (e.g., Molnar & Lyoncaent, 1989; Rothery & Drury, 1984), it is unclear how much deformation there is on these

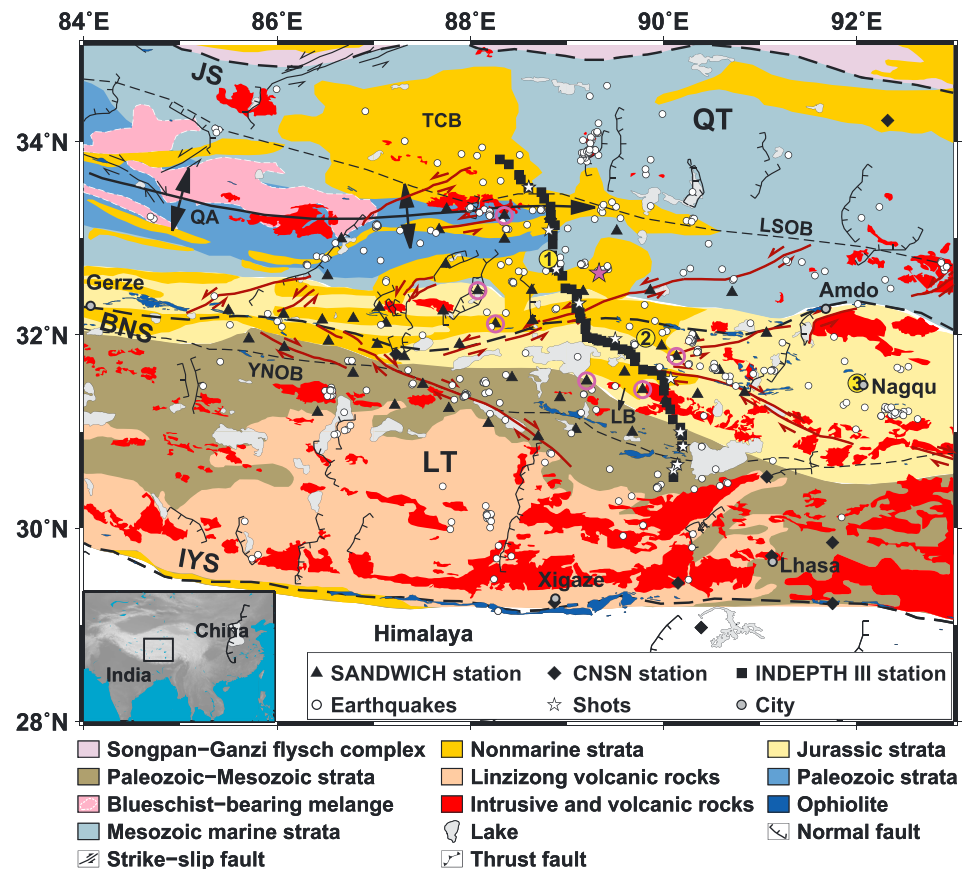


Figure 1. Simplified geological map of the study area with major geological structures, seismic stations, earthquakes, and shots. The numbering of shots 1–12 is from south to north. Shots 7 and 8 have the same locations, as do shots 11 and 12. The geological map has been compiled from Kapp et al. (2005), Wang et al. (2013), and Zhang et al. (2010). Bold dashed black lines are three suture zones in the study area: Bangong-Nujiang suture (BNS), Jinsha suture (JS), and Indus-Yalu suture (IYS). Two thin dashed black lines are ophiolitic belts: Yongzhu-Namtso ophiolitic belt (YNOB) and Longmu Co-Shuanghu ophiolitic belt (LSOB). Bold black line: QA = Qiangtang anticline; QT = Qiangtang terrane; LT = Lhasa terrane; TCB = Tug Co basin; LB = Lunpola basin. Dark-red lines: V-shaped strike-slip fault system. Purple star: The location of the earthquake shown in Figure 3. Purple-circled triangles: The locations of the recording stations shown in Figure 3. Yellow dots with numbers “1, 2 and 3”: The locations of heat flow measurements in central Tibet (He et al., 2014; Jiang et al., 2016; Wang & Huang, 1990). The box in the inset map shows our study area in the Tibetan plateau. The locations of structures are from Kapp et al. (2005), Styron et al. (2010), and Taylor and Yin (2009).

faults. Different modes of deformation have been proposed according to the assumed roles of these faults. In the rigid block (RB) model, the different geological units are considered as rigid blocks, and the deformation occurs mainly along boundary faults with little or no deformation inside the fault-bounded blocks (e.g., Armijo et al., 1989; Peltzer & Saucier, 1996; Rothery & Drury, 1984; Ryerson et al., 2007; Tapponnier et al., 1982; Taylor & Peltzer, 2006; Thatcher, 2007). In contrast, in the continuous deformation (CD) model, deformation is widely distributed over the entire Tibetan plateau (e.g., England & McKenzie, 1982; England & Molnar, 1997; Liang et al., 2013; Wang et al., 2001; Zhang et al., 2004). The alternative is a combination of the RB and CD models spatially or temporally. Either distributed deformation is as important as slip on the major faults as suggested by GPS observations (Chen et al., 2004) or the deformation might be dominated by the RB or CD modes at different developmental stages and in different regions of the Tibetan plateau (Gan et al., 2007). However, the aforementioned deformation mechanisms are mostly based on surface observations, such as velocity fields from GPS data (Chen et al., 2004; Gan et al., 2007; Liang et al., 2013; Thatcher, 2007; Wang et al., 2001; Zhang et al., 2004), slip rates of faults from geomorphic measurements (Armijo et al., 1989; Ryerson et al., 2007; Taylor & Peltzer, 2006), and interpretations of geologic observations (Rothery & Drury, 1984).

The V-shaped conjugate strike-slip faults lie along the BNS from the northern Lhasa terrane to the southern Qiangtang terrane (Figure 1). Previous investigations indicated that northeast trending strike-slip faults on the north side of the BNS are left-lateral faults, whereas southeast trending strike-slip faults on the south side of the BNS are right-lateral faults. The termination points of the conjugate strike-slip faults are linked with NNE striking normal faults in the Qiangtang terrane and north-south trending rifts in the Lhasa terrane, respectively (Armijo et al., 1986, 1989; Taylor et al., 2003). Yin and Taylor (2011) proposed a paired general-shear model to explain the formation of the V-shaped conjugate strike-slip fault system. In their model, the continuous convergence between the Indian and Eurasian plates and the basal shear from eastward asthenospheric flow generated lithospheric paired general shear along the BNS and then caused the development of the conjugate strike-slip faults in central Tibet. However, there are few crustal structure images to constrain the potential mechanism for the formation of the conjugate strike-slip fault system and to improve our understanding of synchronous development of extensional structures in the orogen.

During the past two decades, several geophysical investigations have been conducted along profiles to detect the crustal structure of central Tibet, including the Sino-French program (Sapin et al., 1985), the International Deep Profiling of Tibet and the Himalaya III (INDEPTH-III) project (Huang et al., 2000), the ANTILOPE profile (Array Network of Tibetan International Lithospheric Observation and Probe Experiments; central line; Zhao et al., 2010), and the SinoProbe project (Gao et al., 2013). These investigations have revealed significant variations in the crustal structure of central Tibet. The crustal thickness decreases from the Lhasa terrane to the Qiangtang terrane and increases from west to east within the Lhasa terrane (Gao et al., 2013; Zhang & Klemperer, 2005; Zhao et al., 2001, 2010). There is a distinguishable change in Moho depth around the BNS along the INDEPTH-III and SinoProbe profiles (Gao et al., 2013; Shi et al., 2004; Tian et al., 2005). The mean V_p/V_s value in the upper crust estimated from wide-angle seismic data is <1.71 (Min & Wu, 1987; Zhang et al., 2011; Zhang & Klemperer, 2005) and from earthquake data is ~ 1.75 (Langin et al., 2003). The relatively low V_p/V_s ratios were interpreted as evidence for widespread quartz-rich rocks existing in the upper crust. The estimated seismogenic layer in central Tibet is thinner than 25–30 km, which indicates that the middle-lower crust has high temperatures and ductile behavior (Langin et al., 2003; Taylor & Peltzer, 2006; Zhu et al., 2017). Moreover, the high conductivity from middle to lower crust (Solon et al., 2005; Wei et al., 2001) and the midcrustal low-velocity and low- L_g Q regions in the Lhasa terrane indicated the presence of partial melting (Rapine et al., 2003; Xie et al., 2004; Zhang & Klemperer, 2005). However, the V_p models along the INDEPTH-III profile show little evidence for such a layer (Zhao et al., 2001). Along the INDEPTH-III profile, the BNS is characterized by a low- V_p zone extending to ~ 30 -km depth with a width of ~ 50 km (Haines et al., 2003) or ~ 100 km (Zhao et al., 2001). The explanations for it include a fluid-filled fractured zone (Solon et al., 2005; Zhao et al., 2001), a buried sedimentary basin (Zhao et al., 2001), special compositions such as serpentinite or spilitite (Zhao et al., 2001), or metagreywacke (Zhang et al., 2011). However, there are arrival delays (or “jumps”) near the BNS in the travel time diagram based on the different phase recognition for the INDEPTH-III reflection/refraction profile, which have been speculated to be a wide north dipping fault zone (Meissner et al., 2004) or one or more narrow, steeply south dipping low-velocity channels (Solon et al., 2005).

Recent studies have provided many measurements of the crustal structure in central Tibet. However, due to the unevenly distributed linear investigations in central Tibet, further investigations over the whole V-shaped conjugate fault zone are required to reveal its mechanism of formation. We conducted the joint travel time inversion of earthquakes and reflection/refraction data to obtain a 3-D velocity model, and simultaneously, we relocated these local earthquakes with the updated velocity model. Then, we utilized P wave attenuation tomography using the inverted V_p model and relocated earthquakes to get a 3-D Q_p model. Finally, we discussed the velocity and attenuation models of central Tibet and their implications for the evolutionary mechanism of the conjugate strike-slip fault system.

2. Data and Method

2.1. Data and Data Processing

The earthquake waveform data used in the velocity tomography of central Tibet were obtained from two sources: 53 temporary stations (Table S1 in the supporting information) from the SANDWICH (Seismic Array iNtegrated Detection for a Window of Indian Continental Head) seismic network (Liang,

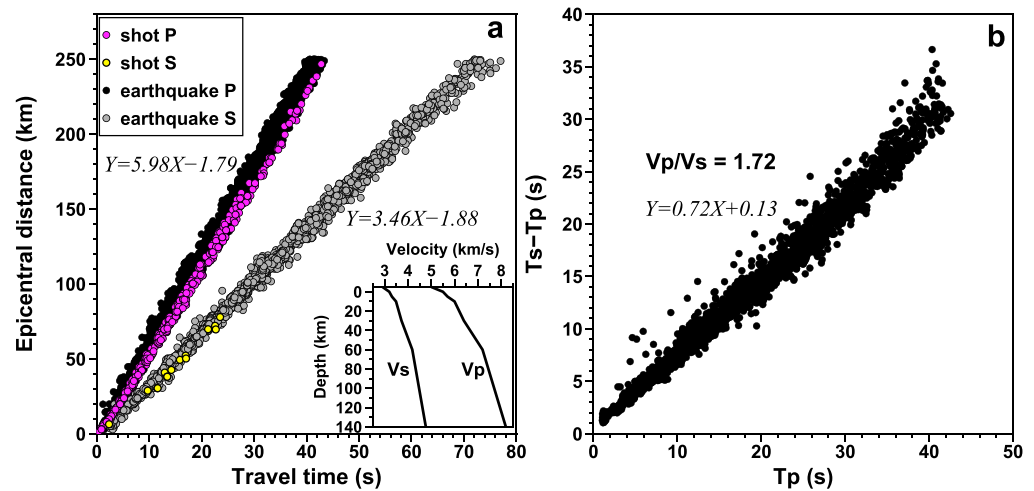


Figure 2. (a) Traveltime versus distance curve for the selected earthquake and shot data; (b) Wadati diagram of arrivals to estimate the average V_p/V_s ratio. The average V_p and V_s estimated for the upper crust in the study area is 5.98 and 3.46 km/s. According to the slope, shot data show lower velocities than earthquake data (the slopes for V_p and V_s of earthquake data are 5.97 and 3.46 km/s, and the slopes for V_p and V_s of shot data are 5.72 and 3.41 km/s, respectively). The initial V_p model (inset figure in a) is derived from the velocity model in Zhao et al. (2001). The initial V_s model (inset figure in a) is calculated using the initial V_p model and the determined V_p/V_s ratio of 1.72.

Tian, et al., 2016) and 10 permanent stations from the China National Seismic Network (CNSN; Data Management Centre of China National Seismic Network, 2007; Zheng et al., 2010). The SANDWICH stations were evenly located on both sides of the BNS from the northern part of the Lhasa terrane to the southern part of the Qiangtang terrane with an average station interval of approximately 40 km (Figure 1). Each station was equipped with a three-component Gralp CMG-3ESP seismometer with a response from 50 Hz to 30 or 60 s and a DAS24-3D or a RefTek 72A-8/130-1 digital recorder (Liang, Tian, et al., 2016). The 10 permanent stations are equipped with 24-bit digitizers and broadband or very broadband seismometers with an instrument response from flat to 60 or 120 s (Zheng et al., 2010).

We collected the waveform data recorded by the SANDWICH and CNSN stations from November 2013 to November 2015. We located 489 local earthquakes using the Hypoinverse-2000 method (Version 1.2) (Klein, 2014) with an initial velocity model from CRUST1.0 (Laske et al., 2013). These events occurred at depths of 0 to 30 km and have local (Richter) magnitudes ranging from 1.0 to 5.3 ML (Zhu et al., 2017). The arrival times of the Pg and Sg phases were manually picked on the vertical and horizontal components, respectively. There are two parts to the Pg and Sg phase data: from November 2013 to November 2014 (Zhu et al., 2017) and from November 2014 to November 2015 (newly processed). We only used Pg and Sg phases with a source-receiver distance shorter than 250 km to eliminate Pn (Sn) phases (Liang, Tian, et al., 2016). There are at least 4 Pg and 3 Sg arrivals for each selected event. As a result of this selection, the final data set consists of 6,817 Pg and 2,929 Sg arrivals from 414 earthquakes (Figure 2a). The hypocenter depths of these selected events mostly range from 0 to 20 km. Hypoinverse does not take account of station elevations, and all stations are on the surface of the Earth. Therefore, those determined earthquake depths are relative to the averaged station elevation, which is about 4,713 m. In other words, the hypocenter depth of 0 km here refers to the averaged station elevation. These hypocenter depths have been converted to depths relative to mean sea level (MSL) in the tomography inversion.

For the velocity inversion, we also included shot data from the INDEPTH-III reflection/refraction experiment. The ~400-km-long INDEPTH-III active-source seismic profile had been conducted from the northern Lhasa terrane to the southern Qiangtang terrane during the summer of 1998. There were 50 three-component broadband and short-period seismographs along the profile with a spacing from 5 to 10 km (Figure 1). We gathered 298 Pg and 15 Sg picks from 12 shots recorded by 46 seismographs (Table S2 and Figure 2a; Mechie et al., 2004). All the shots were placed at a depth of 20 m, and the charge sizes of these shots ranged from 180 to 1,160 kg.

For the attenuation inversion, we only used earthquake waveform data recorded by the SANDWICH network. We removed the instrument responses from the raw waveform data of relocated earthquakes

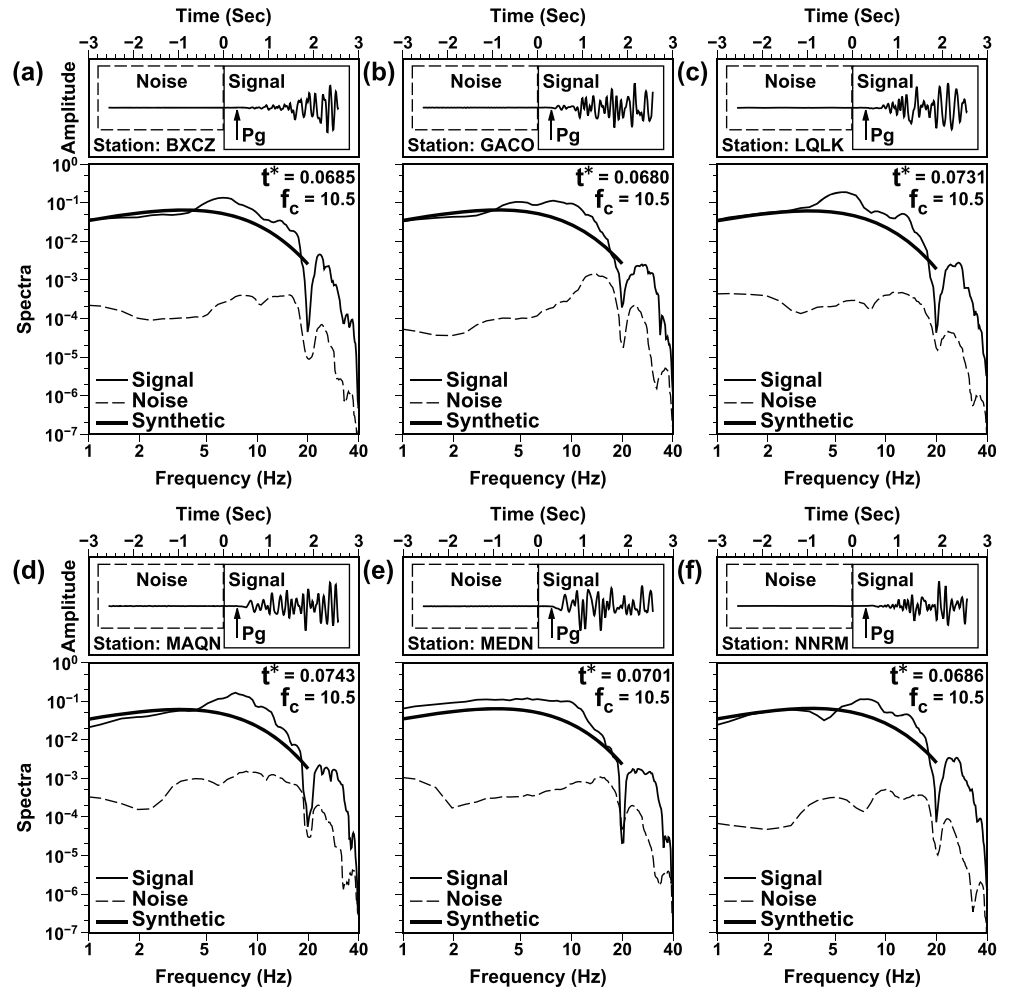


Figure 3. Examples of waveforms (top) and corresponding amplitude spectra (below) for one earthquake recorded by six stations (a–f). This earthquake (latitude, 32.6608 °N; longitude, 89.3057 °E; depth, 3.42 km; magnitude, 3.2 ML; original time, 18:16:57.710, 30 November 2013) is marked as a purple star in Figure 1, and the six stations are marked as purple-circled black triangles in Figure 1. The picked Pg arrivals are marked with small arrows in the figure. The actual noise and signal windows are shown as dashed and bold rectangles, respectively. The amplitude spectra calculated from the observed data are shown under the corresponding waveform for each station, together with the theoretical fit. The best fitting source corner frequency (f_c) for this earthquake and t^* measurement along each raypath are shown in the figure.

and chose vertical-component waveforms of Pg phases. Then we extracted a 2.56-s time window after each Pg arrival as the signal and another 2.56-s time window before the Pg arrival as noise. Due to the uncertainty of phase picking, we set the actual signal time windows to start 0.3 s prior to the Pg arrival, as shown in Figure 3. Then we adopted the multitaper approach from Prieto et al. (2009) to calculate the corresponding amplitude spectrum of the signal and noise time series. We followed the approach outlined in Rietbrock (2001) and Eberhart-Phillips and Chadwick (2002) to determine t^* measurements. According to the theory in Scherbaum (1990), the theoretical amplitude spectrum for a Brune-type source model (Brune, 1970) can be described as

$$A_{ij}(f) = 2\pi f \Omega_{oij} \frac{f_{ci}^2}{f_{ci}^2 + f^2} e^{-\pi f t_{ij}^*}, \quad (1)$$

where $A_{ij}(f)$ is the velocity amplitude spectrum of event i observed at station j , f is frequency, Ω_{oij} is the spectral level, f_{ci} is the source corner frequency, and t_{ij}^* is the t^* value along the raypath from event i to station j . Here we did not use station parameters for avoiding trade-offs between station parameters and other model

parameters. Furthermore, resolvable shallow attenuation structure might be included in station parameters, which is not our preference. We performed an iterative fitting approach described in Lin (2014) to determine the three unresolved parameters: Ω_{oij} , f_{ci} , and t_{ij}^* values. The corner frequency f_{ci} of each event was searched for, over the frequency range, by minimizing the average difference between the calculated and observed velocity amplitude spectra:

$$fit = \frac{1}{N} \sum_{j=1}^N \{ \log[A_{ij}(f)] - \log[D_{ij}(f)] \}^2, \quad (2)$$

where N is the number of observations and $A_{ij}(f)$ and $D_{ij}(f)$ are calculated and observed velocity amplitude spectra, respectively. The determined f_{ci} was used to estimate the final Ω_{oij} and t^* values. For one earthquake, the amplitude spectra are fitted with the same source corner frequency (f_c) and different t^* measurements along the paths from the event to the stations (Figure 3). The t^* values are weighted with weights of 0, 1, 2, 3, and 4, indicating quality of fitting from the best to the worst. In the fitting approach, we only used a spectrum from 0 to 20 Hz with a signal-to-noise ratio greater than 2 over a continuous frequency band wider than 10 Hz (Figure 3). In the end, we obtained 2,699 t^* values from 237 earthquakes for the Qp tomography inversion (Figure S1).

2.2. Velocity Tomography and Earthquake Relocation

In this study, we applied the SIMUL2000 tomography algorithm (Eberhart-Phillips, 1993; Thurber, 1983, 1993; Thurber & Eberhart-Phillips, 1999) to invert for Vp and Vp/Vs, relocate earthquakes, and then invert for Qp model. The pseudo-bending ray-tracing method and the damped least squares inversion approach are used in this code, and thus, the final tomographic results depend on the selection of the inversion parameters, such as grid spacing, initial model, and damping parameters.

A flexible gridding strategy for initial model parameterization based upon the distribution of events and stations has been adopted in the code (Thurber & Eberhart-Phillips, 1999). In the velocity tomography, we parameterized our research region by a three-dimensional mesh with $25 \times 19 \times 9$ grid nodes after multiple checkerboard tests. The center of the Cartesian coordinate system is set at 31.75°N , 88.83°E , and the x -axis and y -axis point to the west and north directions, respectively. We set the interior grid spacing to 30 km and the marginal grid spacing to 60 km in the horizontal direction (Figure 4). The nodes in the vertical direction are positioned at depths of -5 , 0, 5, 10, 15, 20, 30, 60, and 140 km. Although the models between 30- and 140-km depth could not be inverted, they are essential for the travel time calculations in the ray tracing procedure.

We used a 1-D layered Vp model from the average of the local velocity model presented by Zhao et al. (2001) as the initial Vp model (inset figure in Figure 2a). A constant Vp/Vs ratio of 1.72 was determined as the initial Vp/Vs value based upon the Wadati diagram of our travel time data (Figure 2b). This value is within the results estimated by previous studies (Langin et al., 2003; Min & Wu, 1987; Zhang et al., 2011; Zhang & Klemperer, 2005). Note that the depth of 0 km in the initial model represents MSL and in the following content all depths are relative to MSL. Therefore, the locations of the earthquakes and shots used were adjusted to depths relative to MSL.

We determine the optimal damping parameters for Vp and Vp/Vs using an empirical iterative approach. We ran a series of single-iteration inversions with different damping values and selected the final ones based on the trade-off between data misfit and model variance. A range of values from 1 to 5,000 was tested to make sure that the range is large enough to include the most appropriate one (Evans et al., 1994). At first, we selected Vp damping using both P and S wave data with Vp/Vs damping kept at a very large value. A preferred Vp damping of 800 was chosen based on a balance between data misfit and model perturbation, which means a proper data misfit with a modest complicated model (an appropriate model variance). Then we similarly selected Vp/Vs damping with Vp damping fixed at 800. An optimal Vp/Vs damping of 100 was chosen. Finally, we reran a set of single-iteration inversions using different Vp damping values while Vp/Vs damping was held at 100 in order to check the applicability of 800 as the Vp damping (Lin et al., 2014). We found that 800 is an appropriate value for Vp damping in the above case (Figure S2).

There is always a trade-off between velocity structure and source parameters, which can be amended by the iterative determination of velocity model and earthquake locations (Shearer, 2009). We inverted Pg and

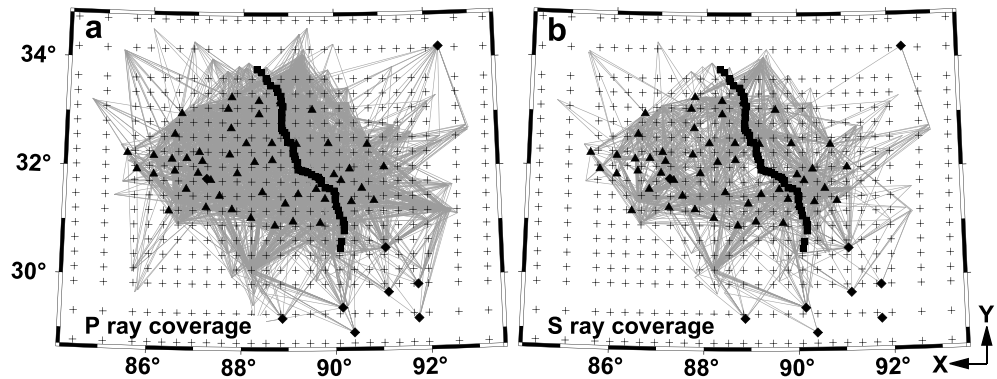


Figure 4. Inversion grid nodes (gray crosses) and horizontal ray coverage (gray lines) for *P* (a) and *S* (b) data used in the velocity tomography in plane view. Triangles (Seismic Array Integrated Detection for a Window of Indian Continental Head array), diamonds (China National Seismic Network), and squares (International Deep Profiling of Tibet and the Himalaya III profile) denote recording stations.

Sg-Pg travel times for preliminary V_p and V_p/V_s models and relocated the earthquakes with these preliminary velocity models. We then inverted for velocity models again with these improved source parameters. Then the newly updated velocity models were used to relocate the earthquakes once again. We continually performed this velocity inversion-earthquake relocation loop until the earthquake locations remained relatively constant and the root mean square (RMS) of the travel time residuals reached a minimum. We calculated the changes of earthquake locations from each iteration (i^{th}) to the next one ($[i + 1]^{\text{th}}$). The mean value of the changes fluctuated around ~ 0.5 km (~ 0.3 km in horizontal and vertical directions; Figure S3), and the RMS of the travel time residuals reached a steady value for both earthquakes and shots after 10 iterations (Figure S4). This indicates that the uncertainty of the final earthquake locations was ~ 0.5 km (~ 0.3 km in horizontal and vertical directions). After the velocity inversion-earthquake relocation loops, the residual RMS of the earthquake data decreased by 56.9% from 1.16 to 0.50 s (Figure S4a), and the residual RMS of the shot data decreased by 46.4% from 0.56 to 0.30 s (Figure S4b). The histograms show that the initial residuals trended toward the negative side for earthquakes but trended slightly toward positive values for the shot data (Figure 5). This is because the initial 1-D velocity model is from the wide-angle reflection/refraction study, which usually provides good-quality images but lower velocities near the surface of the Earth than passive-source seismic studies

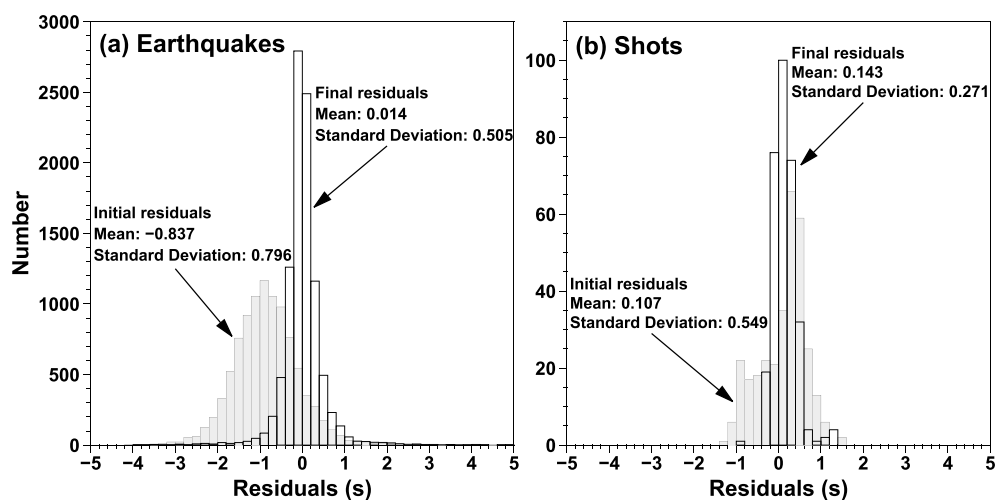


Figure 5. Histograms of traveltimes residuals for earthquakes (a) and shots (b) before (gray) and after (white-black) the velocity inversion-earthquake relocation loop. The initial residuals trend toward the negative side for earthquakes (a) but trend slightly toward a positive value for shots (b).

(Figure 2a). The SIMUL2000 program calculates the absolute location uncertainties in x , y , and z directions as the largest of the principal standard errors for each earthquake. After the final loop, the median of the overall location uncertainties is 81 m in the horizontal direction and 220 m in the vertical direction. The relocation result (Table S3) shows tighter clustering of the events than the original locations (Figure S5).

In order to have another estimation of the location errors of the earthquakes, we located all the shots using the final Vp and Vp/Vs models. A similar assessment had been done previously but not for all the shots (Langin et al., 2003). Figure S6 shows the difference between the relocations and actual locations of the shots in the horizontal (a) and vertical (b) directions. Of the 12 shots, 11 have location errors less than 2 km (dots in the dashed line squares), and only one shot has location errors as high as 6.4 km. Moreover, the location errors in the x direction (east-west) are prone to be larger than in the other directions, since all the shots and seismographs were distributed along an approximately y -direction (north-south) profile (Figure 1). On average, the epicenter error is about 1.54 km, and the vertical error is about 0.90 km. The azimuthal gaps of shots 2–12 range from 150° to 220°, whereas shot 1 has a larger azimuthal gap of 320°. Myers et al. (2015) showed that epicenter errors increase nearly linearly with azimuthal gap between 0° and 220°, and nonlinearly when the azimuthal gap is larger than 220°. The local earthquakes were recorded by 2-D seismic arrays and have better azimuthal coverage than the shots. However, earthquakes cannot be located as well as explosions under the same conditions, since earthquakes are more complicated (Bondar et al., 2004). All in all, in view of the lack of azimuthal coverage and S wave phase data for the shots, the location errors are likely to represent the maximum errors in the earthquake relocation. This is further substantiated by the fact that the errors derived from shot relocations are larger than the location uncertainties estimated by the SIMUL2000 program.

2.3. Attenuation Tomography

After the velocity inversion, we performed the local attenuation tomography using t^* measurements from the vertical component waveforms of the relocated earthquakes. With a set of t_{ij}^* values and an a priori 3-D Vp model, we can derive a Qp model from the following equation:

$$t_{ij}^* = \frac{t_{ij}}{Q_{ij}} = \int \frac{1}{Q_p(x,y,z) * V_p(x,y,z)} ds, \quad (3)$$

where ds is a segment of path length and $Q_p(x,y,z)$ and $V_p(x,y,z)$ are Qp and Vp values along the segment, respectively. The SIMUL2000 tomography algorithm (Rietbrock, 1996; Thurber & Eberhart-Phillips, 1999) was used to invert the t^* values for Qp models by minimizing the weighted RMS of t^* residuals.

In the attenuation tomography, we parameterized the 3-D Qp model with a grid spacing of 60 km in the interior and 120 km in the marginal regions in the horizontal direction due to fewer t^* measurements than travel times (Figure S1). The nodes in the depth direction are the same as in the velocity tomography. We performed ray tracing through the obtained Vp model. The initial Qp model was determined according to the procedure in Lin (2014). We searched the initial uniform Qp through a sequence of values from 100 to 2,000 with an interval of 50. We calculated the RMS of t^* residuals using these models and evaluated the correlation between the Qp values and RMS residuals. Then we chose 500 as the initial uniform Qp, since the RMS residual at this point is a minimum (Figure S7a). After this, we ran a series of single-iteration inversions beginning with Qp = 500. In each iteration, the average results of the previous layer values were used as the initial model for the next iteration. We continually ran the inversion until the layered Qp model remains relatively constant. The final layered model served as the initial model in the final Qp tomography (Figure S7b). We selected an optimal damping parameter for Qp with a similar method as was used in the velocity inversion. We ran a sequence of single-iteration inversions with a damping value increasing from 0.005 to 1 and then chose a Qp damping of 0.014 for the Qp inversion, which produces a reasonable trade-off between data misfit and model perturbation (Figure S8). The Qp tomographic inversion converged after five iterations, and the RMS of the t^* residuals decreased by 9% (Figure S9).

3. Resolution Test

We carried out checkerboard tests to assess the spatial resolution of the velocity and attenuation models. In the resolution tests, the locations of events and stations, the utilized event-station pairs, the initial models,

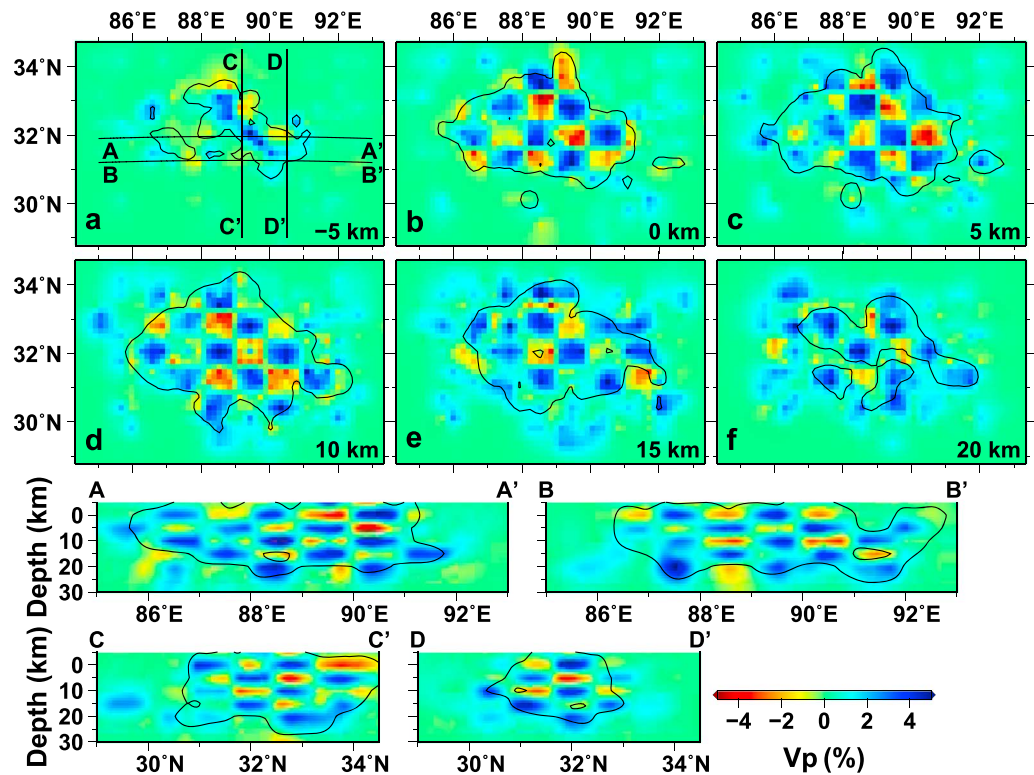


Figure 6. (Upper) Results of checkerboard test for V_p in horizontal slices at depths of -5 , 0 , 5 , 10 , 15 , and 20 km (a–f). (Down) Results of checkerboard test for V_p in vertical slices shown in subplot a (A–A', B–B', C–C', and D–D'). Synthetic travel times were computed by using the layered initial model with $\pm 5\%$ perturbations that are two grid spacings (2×30 km) in size, horizontally, and alternately distributed at adjacent depths. The black contours enclose the regions with derivative weighted sum greater than 900, where the checkerboards show the potential ability to recover the models.

and inversion parameters are exactly the same as in the real data inversions. Synthetic travel times were computed by using the layered initial model with $\pm 5\%$ V_p and $\pm 5\%$ V_p/V_s perturbations that are two grid spacings (2×30 km) in size and alternately distributed at adjacent depths. Likewise, synthetic t^* values were computed by using the initial model with $\pm 20\%$ Q_p perturbations, which are also two grid spacings (2×60 km) in size and alternately distributed at adjacent depths. Then we inverted the synthetic data and evaluated how well the checkerboard models were recovered. Although there is smearing at the margins, the V_p checkerboards are generally recovered between -5 - and 20 -km depths (Figure 6). Since we have less S wave data than P wave arrivals, the V_p/V_s checkerboard model is recovered only between 0 - and 10 -km depths (Figure 7). Owing to the limited t^* measurements, the resolution of the Q_p model is expected to be not as good as the V_p structure. The Q_p checkerboards are reconstructed from -5 - to 20 -km depths (Figure 8). The derivative weighted sum (DWS) describes the relative raypath density that is weighted by ray segment length and its distance to each node (Evans et al., 1994). We found that the regions with DWS greater than 900 were well recovered, so we showed the results only for $DWS > 900$ in the final presentation.

We also performed customized model recovery tests to investigate the reliability of the obtained V_p and V_p/V_s features (Figures S10 and S11). Input models were intentionally designed with perturbations similar to anomalies in the inversion results. In Figure S10, the input models include low V_p anomalies at -5 - to 10 -km depths (a–d) and high V_p/V_s anomalies at 0 -km depth (e). All the input anomalies were generally recovered, but with decreased magnitude (f–j), especially for images at -5 -km depth (f). The recovered image of a belt of low V_p at 0 -km depth (g) shows slight vertical smearing at adjacent depth layers (f and h). In Figure S11, the locations of the profiles are the same as in Figure S12. Based on this customized model recovery test, both the obtained low V_p and high V_p/V_s anomalies are deduced to be robust features.

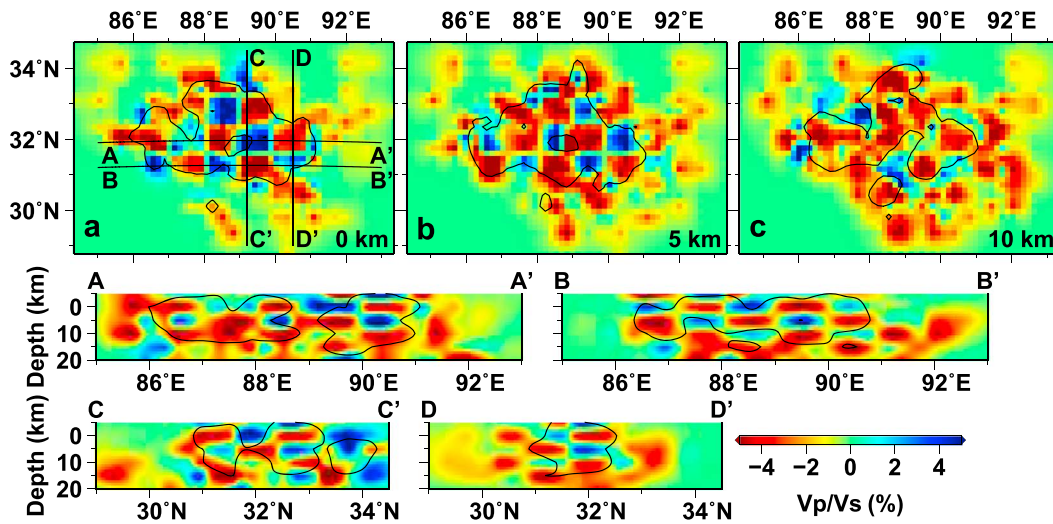


Figure 7. (Upper) Results of checkerboard test for V_p/V_s ratio in horizontal slices at depths of 0, 5, and 10 km (a–c). (Down) Results of checkerboard test for V_p/V_s ratio in vertical slices shown in subplot a (A–A', B–B', C–C', and D–D'). The V_p/V_s perturbations were $\pm 5\%$ in amplitude, had horizontal dimensions of two grid spacings (2×30 km), and were alternately distributed at adjacent depths. The black contours have the same meaning as in Figure 6.

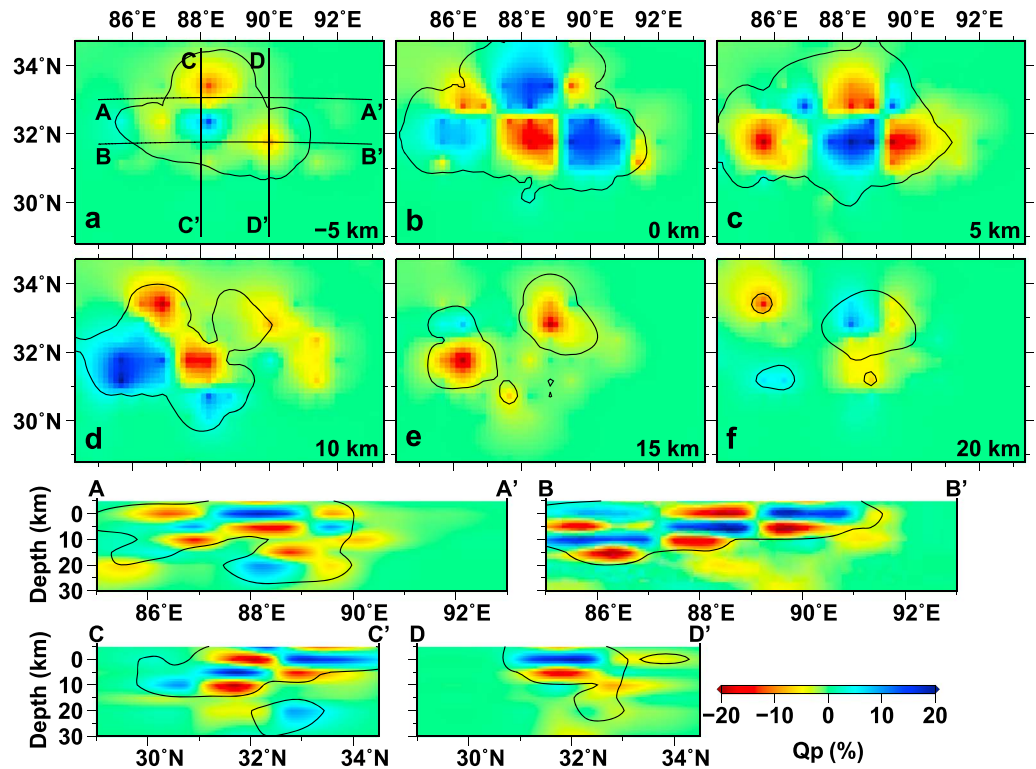


Figure 8. (Upper) Results of checkerboard test for Q_p in horizontal slices at -5 -, 0 -, 5 -, 10 -, 15 -, and 20 -km depths (a–f). (Down) Results of checkerboard test for Q_p in vertical slices shown in subplot a (A–A', B–B', C–C', and D–D'). Synthetic f^* values were computed by using the initial model with $\pm 20\%$ perturbations, which are two grid spacings (2×60 km) in size, horizontally, and alternately distributed at adjacent depths. The black contours have the same meaning as in Figure 6.

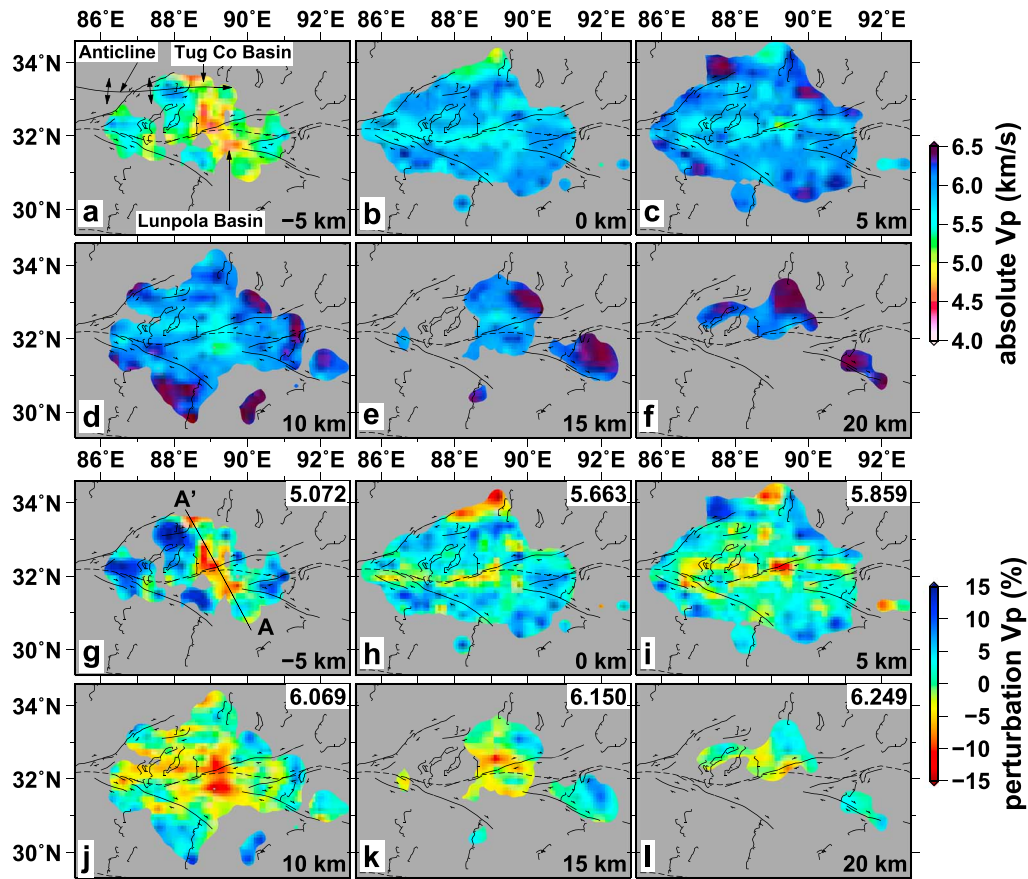


Figure 9. Final Vp structures at depths of -5 , 0 , 5 , 10 , 15 , and 20 km in absolute values (a–f) and perturbations (g–l) relative to the mean value at each depth. The A–A' in g is the location of the International Deep Profiling of Tibet and the Himalaya III profile, and the numbers in the top-right corner of g–l are the mean Vp (km/s) at each depth. We only show the results in regions with the derivative weighted sum greater than 900, where the inverted model is more reliable (Figure 6). The black lines and dashed lines denote fault traces and sutures at the surface, respectively.

4. Results

The main feature in the tomographic results is a prominent low Vp and Vp/Vs ratio zone from the surface to 10-km depth. This low Vp and Vp/Vs zone extends right along the BNS and narrows to 20 km at shallower depth (0 km) but broadens to 100 km in the north-south direction at greater depth (10 km; Figures 9, 10 and 11). This feature is consistent with previous results from investigations along linear profiles (Haines et al., 2003; Zhao et al., 2001). The results also reveal a slight decrease in the Vp/Vs ratio from 0- to 10-km depth. At 0-km depth, the Vp/Vs ratio is dominated by high values (>1.75), whereas at 5- to 10-km depth the Vp/Vs ratio is relatively low between 1.6 and 1.7 (Figure 10).

There are other relatively low Vp anomalies near the surface in the study area (Figure 9). One of them is located at -5 -km depth along the INDEPTH-III profile (Figure 11a), which is spatially correlated with the Lunpola basin. Another shallow low Vp zone ranges in depth from -5 to 0 km in the Tug Co basin. These low Vp zones are spatially correlated with the major sedimentary basins in the research region and might reflect the thick sedimentary strata in these basins (Zhang et al., 2010). The only mismatch is a strong high Vp anomaly in the Tug Co basin, which is probably due to the raised Qiangtang anticline with shallow burial (Kapp et al., 2005; Lu et al., 2013; Figure 1). Other high Vp anomalies are strongly related to the solidified sediments and metamorphic rocks in Zhang et al. (2010). Moreover, the edge of the Tug Co basin shows a high Vp/Vs ratio (>1.80 ; Figures 10a and 10d) with a relatively low Vp anomaly at 0-km depth (Figures 9b and 9h). These subregions probably indicate the existence of fluid accumulations.

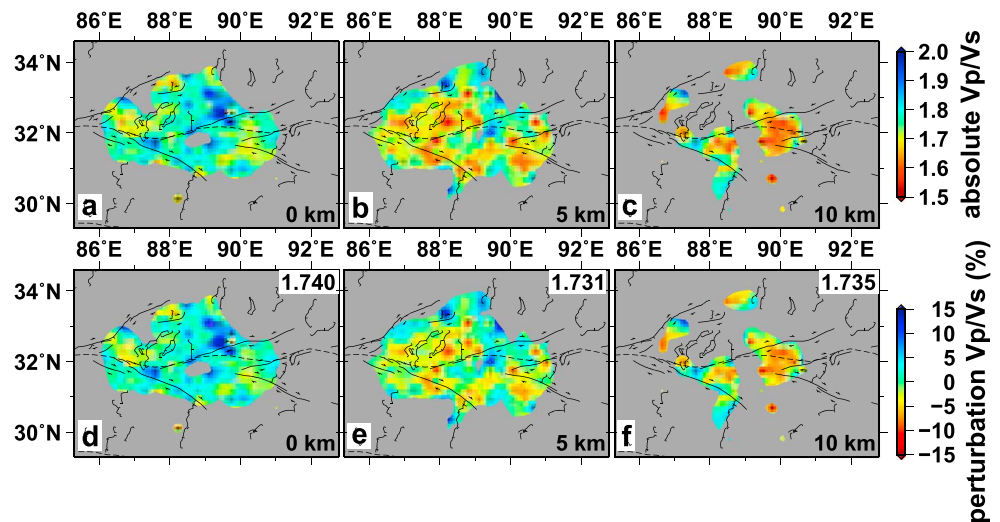


Figure 10. Final Vp/Vs ratios at depths of 0, 5, and 10 km in absolute values (a–c) and perturbations (d–f) relative to the mean value at each depth. The numbers in the top-right corner of d–f are the mean Vp/Vs ratios at each depth. Other symbols are the same as in Figure 9.

There is also a low Vp anomaly at 10-km depth beneath the INDEPTH-III profile around the BNS (Figures 9d, 9j, and 11). A low Vp/Vs ratio anomaly occurs at about the same location, though the resolution is quite limited at this depth (Figures 10c, 10f, and 11). Another apparent low Vp anomaly is continually present from 0- to 10-km depth around the largest earthquake cluster zone (33.8°N, 89.2°E; Figures 9b–9d and 9h–9j; Zhu et al., 2017). The Vp/Vs ratios show a transition from high Vp/Vs ratios at 5-km depth to low Vp/Vs ratios at 10-km depth for this region (Figures 10b, 10c, 10e, and 10f).

The average Vp/Vs ratio of the whole upper crust is 1.72 (Figure 2b). This estimate of the mean value is higher than the results from the Sino-French (<1.70) and INDEPTH-III (1.63–1.71) wide-angle profiles (Mechie et al., 2004; Min & Wu, 1987; Zhang et al., 2011; Zhang & Klemperer, 2005), but a little lower than the value of ~1.75 estimated in Langin et al. (2003). Obviously, the estimation in Langin et al. (2003) and our results partly include data from the middle crust. The difference between these results implies that Vp/Vs ratios vary quite significantly in the crust of central Tibet.

The Qp results present complicated patterns (Figure 12). The Qp values from –5- to 5-km depths range from 100 to 800, while from 10- to 20-km depth they vary from 200 to 1,400. The Qp values change dramatically in the study area. We note that seismogenic regions generally show low Qp values and high Qp regions often correspond to seismicity gaps. The low-Qp feature along the INDEPTH-III profile (Figure 11c) is similar to the low-Lg Q anomalies, which were interpreted as being due to partial melting and high temperature in the crust (Xie et al., 2004).

5. Discussion

5.1. Low-Velocity Belt Along the BNS

Seismic velocity is associated with various factors, such as rock type, confining and pore pressure, temperature range, porosity, fluid content, and geological age. The most prominent feature in the tomographic results is the 80- to 100-km-wide low-velocity zone along the BNS from 0- to 10-km depth. The maximum depth of this anomaly might be greater, but we do not have more data to constrain it. The signature agrees well with the low-velocity zone found in previous research, but our results show a clear spatial distribution of this anomaly, which is better than the results from the linear reflection/refraction profiles (Haines et al., 2003; Meissner et al., 2004; Zhao et al., 2001). Further, this low-velocity zone is also spatially correlated with the high resistivity zone in the upper crust around the BNS (Figures 11a and 11d; Solon et al., 2005).

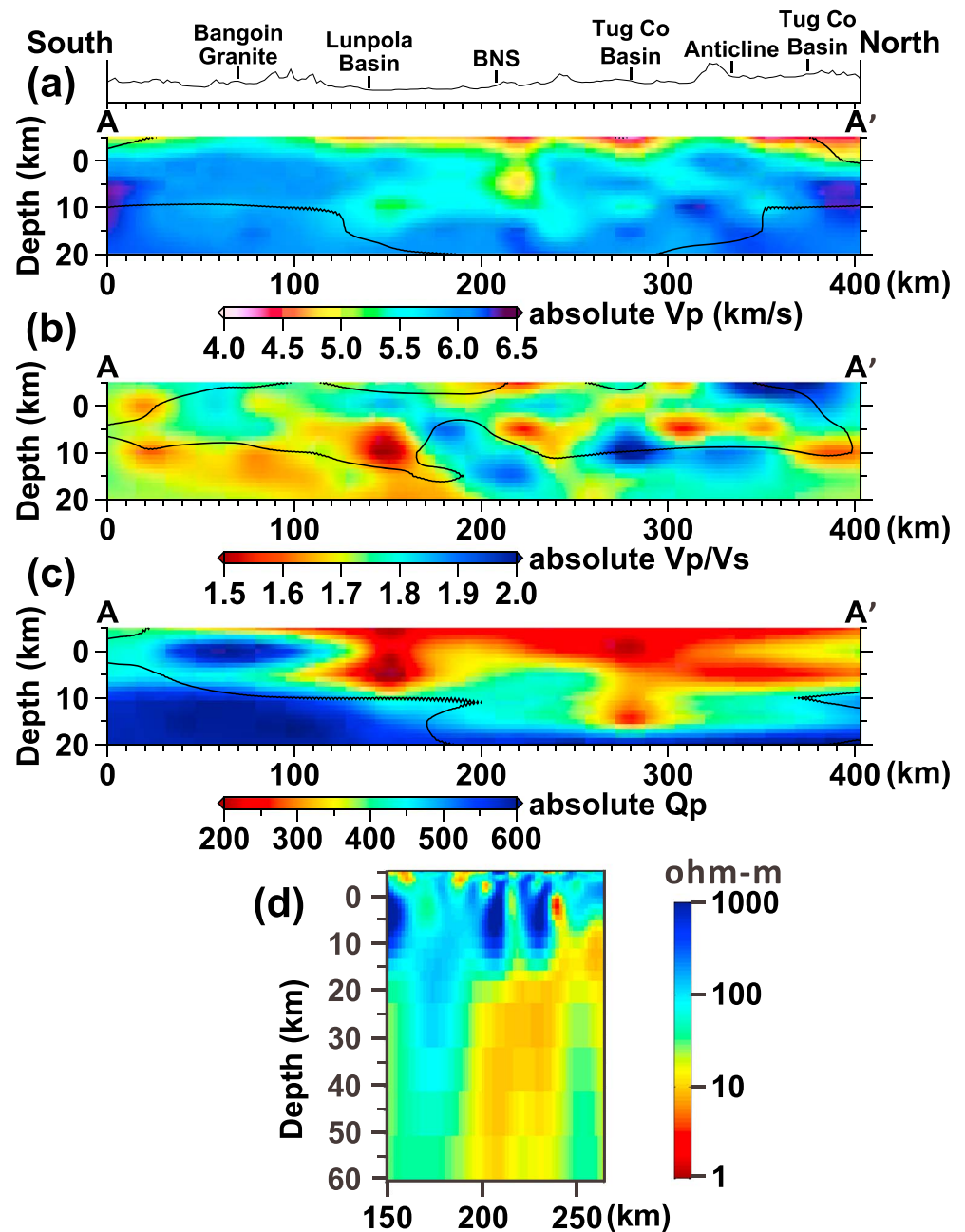


Figure 11. Vertical sections of Vp (a), Vp/Vs (b), Qp (c), and resistivity (d) structures in absolute values along the International Deep Profiling of Tibet and the Himalaya III profile (A-A' in Figure 9g). The black contours enclose the regions with the derivative weighted sum greater than 900. The Vp, Vp/Vs, and Qp models (a-c) are from this study, and the resistivity model (d) is from Solon et al. (2005) at the corresponding location. There is a little difference between the locations of the profiles in Solon et al. (2005) and our study. BNS = Bangong-Nujiang suture.

There are several factors probably causing the low-Vp zone around the BNS, including high temperature, fluids, and compositional variation. High temperature could be one potentially important factor for the low velocity since the heat flow is high around the BNS (Wang & Huang, 1990). The shallow seismogenic depth (25- 30-km depth) in central Tibet (Langin et al., 2003; Taylor & Peltzer, 2006; Zhu et al., 2017) also reflects a high thermal gradient (Chen & Molnar, 1983). There are only three heat flow measurements around our research region in central Tibet (Figure 1), with two of them being reliable as 46.7 mW/m² (category A, referring to Wang & Huang, 1990) and 140 mW/m² (category B, referring to Wang & Huang, 1990)

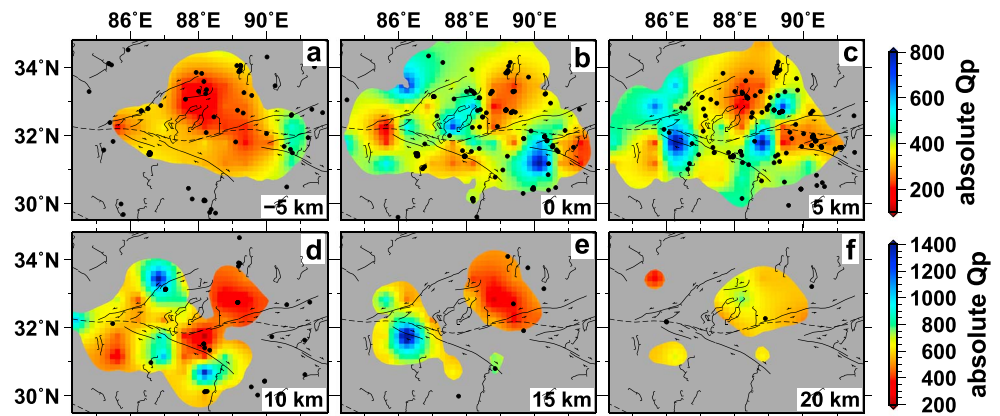


Figure 12. Final Q_p structures at depths of -5 , 0 , 5 , 10 , 15 , and 20 km in absolute values (a–f). The black dots mark the earthquakes that occurred within ± 2.5 km of each depth. Different color scales are used for a–c and d–f. Other symbols are the same as in Figure 9.

for the Tug Co (Qiangtang) and Lunpola basins, respectively (Jiang et al., 2016). The thermal gradients are ~ 15.5 $^{\circ}\text{C}/\text{km}$ with an average vertical thermal conductivity of 3.01 $\text{W}/(\text{m K})$ in the center of the Qiangtang basin (He et al., 2014) and ~ 55.5 $^{\circ}\text{C}/\text{km}$ with an average vertical thermal conductivity of 2.51 $\text{W}/(\text{m K})$ in the Lunpola basin (Wang & Huang, 1990). However, indirect estimations of thermal gradients are 25 $^{\circ}\text{C}/\text{km}$ in the Lhasa terrane and 39 $^{\circ}\text{C}/\text{km}$ in the Qiangtang terrane from the α - β quartz transition in the upper crust, manifested as a P wave velocity increase of 0.2 – 0.4 km/s accompanied by only a minor change in S wave velocity (Mechie et al., 2004). The relatively high geothermal gradient agrees well with relatively low velocity and high attenuation along the INDEPTH III profile (Figure 11), although these two estimations seem opposite for the transition from the Lhasa to Qiangtang terranes. On the other hand, if the two measured heat flow values around this region are considered as two end members, we can estimate the possible velocity variations due to high temperature. The high thermal gradient in the low-velocity zone (Lunpola basin) would give a temperature of about ~ 550 $^{\circ}\text{C}$ at 5 -km depth (below MSL or 10 km below the surface). Similarly, the low thermal gradient outside the low-velocity zone (Tug Co basin) would give a temperature of ~ 150 $^{\circ}\text{C}$ at the same depth. This results in a temperature difference of 400 $^{\circ}\text{C}$ between the low-velocity zone and the region outside it at 5 -km depth. In the same way, a temperature difference of 600 $^{\circ}\text{C}$ at 10 -km depth has been estimated. In the upper crust, a temperature difference of 200 $^{\circ}\text{C}$ can account for 0.1 km/s V_p variation (Christensen, 1979). Thus, with respect to temperature alone, the maximum change in V_p would be about 0.2 – 0.3 km/s at 5 - and 10 -km depth in different regions of the study area. This suggests that the low-velocity zone is unlikely to be produced by high temperature alone and there should be significant contributions from fluid and compositional variations. Additionally, the obtained Q_p values at 5 - and 10 -km depths are generally low (< 400) with relatively uneven patches, which agrees with the attenuation in tectonically active regions (e.g., Liang et al., 2014; Mitchell, 1995). Since Q_p is sensitive to temperature and/or fluids, its patchy distribution indirectly confirms that the low-velocity zone along the BNS in central Tibet should not be caused mainly by high temperatures or fluids. This is also supported by the high resistivity upper crust around the BNS (Figure 11d; Solon et al., 2005), which is consistent with a fluid-poor status for the low-velocity zone. Otherwise, a fluid-rich medium would show as high conductivity features.

Alternatively, compositional differences might be an important factor for this low- V_p zone, due to its spatial correlation with the BNS, which was formed by the Lhasa terrane colliding with the Qiangtang terrane during Jurassic-Cretaceous time (Yin & Harrison, 2000). Recent geological research reveals that there might be double-sided subduction along the BNS, because of the existence of two Jurassic-Cretaceous magmatic arcs in the northern Lhasa terrane and southern Qiangtang terrane, which implies that the Bangong Ocean may have closed through arc-arc “soft” collision rather than continent-continent “hard” collision (Zhu et al., 2016). The low- V_p region along the BNS is accompanied by variable V_p/V_s ratios and north-south variably high resistivity (Figure 11d; Solon et al., 2005) around the BNS. These features might reflect the compositional differences in the ophiolitic mélangé zone and the collided magmatic arcs along

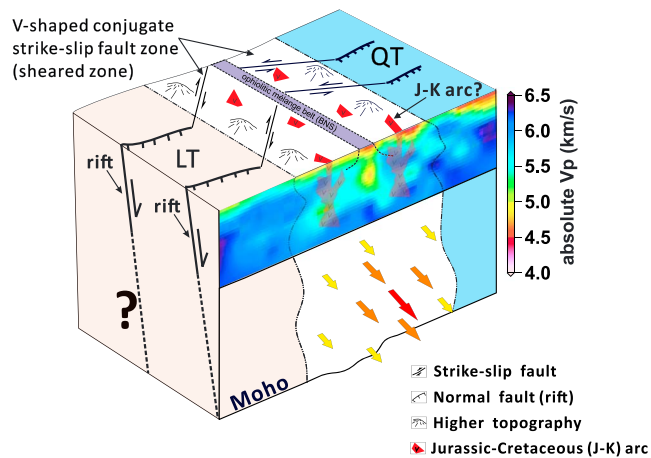


Figure 13. Schematic cartoon overlain by the V_p model along the International Deep Profiling of Tibet and the Himalaya III profile (Figure 11a) for the interpretation of the tomographic results. The QT and LT were sutured along an ophiolitic mélangé belt (BNS) accompanied by two magmatic arcs from a double-sided subduction of the Bangong-Nujiang ocean, which corresponds to our observed low-velocity zone along the BNS. Short arrows (with yellow color), medium arrows (with orange color), and long arrows (with red color) refer to relatively low, medium, and high flow velocities of materials in the middle and lower crust, respectively. The conjugate strike-slip fault zone originates from the north-south contraction and east-west basal shear from middle/lower crust around the BNS. QT = Qiangtang terrane; LT = Lhasa terrane; BNS = Bangong-Nujiang suture.

the BNS (Figure 13). Low V_p/V_s ratios in the upper crust were also found along the Sino-French and INDEPTH-III profiles. Previous research suggests that the relatively low V_p/V_s ratios indicate that quartz-rich rocks (such as granites, granitic gneisses, and granite-granodiorite) widely exist in the upper crust (Figure 1; Min & Wu, 1987; Zhang et al., 2011; Zhang & Klemperer, 2005), which is consistent with the proposed collided magmatic arcs.

Another possibility for the compositional difference is a series of small Cenozoic basins created by the along-suture east-west extension and the overlain deep-seated Jurassic turbidite, interpreted as forearc sediments and/or collision-induced foredeep deposits, around the BNS (Yin & Harrison, 2000). The low velocity might reflect the combination of the two sedimentary units compared with the surrounding strata. However, this possibility can be eliminated because the Jurassic strata are widely exposed in the northern Lhasa and Qiangtang terranes, and not only along the BNS (Figure 1).

Coincidentally, almost half of the earthquakes occurred at 5- to 10-km depth (Langin et al., 2003; Zhu et al., 2017), which corresponds to the depth range where the low V_p zone is most prominent. The Cenozoic tectonic activity, including north-south compression and the development of strike-slip faults, may strongly affect the structure of the upper crust. However, whether the alteration of the upper crustal structure causes the low-velocity zones or the relatively weak materials (ophiolitic mélangé) with low velocities cause the deformation to focus along the BNS is unclear. Since the conjugate strike-slip fault zone has developed uniquely along the BNS, there should be a special initial prerequisite,

likely a weak zone, to stimulate the formation of this sheared zone along the BNS. Then, the later speculation seems more reasonable.

5.2. Formation of the Conjugate Strike-Slip Fault Zone

Generally, the north-south trending normal faulting in the Lhasa and Qiangtang terranes, which is kinematically linked with the conjugate strike-slip fault zone, has been initiated since the Miocene (e.g., Blisniuk et al., 2001; Kapp et al., 2008; Maheo et al., 2007; Murphy et al., 2009; Williams et al., 2001). However, recent dating of north-south trending diabase and andesitic porphyry dikes around the Shuanghu graben provide evidence that the north-south trending normal faulting initiated in the Eocene (47–38 Ma; Wang et al., 2010). Thus, the initiation of the conjugate strike-slip fault system must be later than the collision of the Indian and Eurasian continents at about 65 Ma (Ding et al., 2005). It is reasonable that the low V_p zone distributed on both sides of the BNS implies that uniform stress and continuous deformation occurred in the upper crust of central Tibet due to the relatively weak strength of the region around the BNS under the continuous convergence. This further confirms the possibility of the development of an upper-crustal shear zone around the BNS in central Tibet. Thus, our preferred explanation for the low V_p zone is that a sheared zone developed along the relatively weak ophiolitic mélangé belt around the BNS (Figure 13). The V_p/V_s ratios of the upper crust are relatively low in central Tibet (see above and Figure 10). In contrast, the middle and lower crusts beneath the BNS along the INDEPTH-III profile have a relatively high V_p/V_s ratio of 1.84 (Mechie et al., 2004), and the average V_p/V_s ratio of the whole crust in central Tibet is ~ 1.81 (e.g., Liang, Tian, et al., 2016; Tian et al., 2005). Therefore, we could infer that the V_p/V_s ratios of the middle and lower crusts are relatively high, which in turn implies a ductile middle and lower crust in central Tibet, consistent with the viscosity estimation from postseismic relaxation of two earthquakes (Ryder et al., 2014). In addition, the estimated thickness of not more than 30 km for the seismogenic layer (Langin et al., 2003; Wei et al., 2010; Zhu et al., 2017), the high conductivity from middle to lower crust (Figure 11d) (Solon et al., 2005), the low- V_s zones (Rapine et al., 2003), and the low- L_g Q regions (Xie et al., 2004) in central Tibet all support the idea of a ductile or even partially molten middle and lower crust (Klemperer, 2006).

There is a ductile or even partially molten middle/lower crust along the BNS and other regions of Tibet based on our inferences and previous observations (e.g., Singh et al., 2012; Wei et al., 2001; Zhao et al., 2013). Meanwhile, an upper mantle high velocity anomaly has been observed beneath the BNS from 100 to 250 km (Figure S13) (Liang, Chen, et al., 2016). Thus, we speculate that the shear traction for the formation of the conjugate strike-slip faults is derived from the flow of the middle/lower crust instead of the asthenosphere in central Tibet (Yin & Taylor, 2011). Furthermore, there is a zone where the topography is ~500 m lower than that of the regions to the north and south of it along the axis of the BNS, but there is not a corresponding relatively shallower Moho around the BNS (Figure S13; e.g., Gao et al., 2013; Shi et al., 2004; Tian et al., 2005; Zhao et al., 2001, 2010). This conflict might imply that the middle/lower crust has a different physical status around the BNS, such as lower viscosity compared with the surrounding region. However, the above inferences require further tests, such as the structure and properties of the deeper crust, or even the upper mantle.

Acknowledgments

We would like to thank all the members of the SANDWICH working group for collecting earthquake waveform data for this study. The Seismic Array Laboratory of the Institute of Geology and Geophysics, Chinese Academy of Sciences (SAL-IGGCAS), maintained the instruments for the SANDWICH project. We are also grateful to all the geophysicists who worked on the INDEPTH-III project. The earthquake waveform data from the CNSN were provided by the Data Management Centre of China National Seismic Network at the Institute of Geophysics (SEISDMC, doi:10.11998/SeisDmc/SN), China Earthquake Networks Center and XZ Seismic Networks, China Earthquake Administration. The constructive comments and suggestions from two reviewers and associate editor have improved the manuscript. We thank Alan G. Jones for providing the resistivity model along the INDEPTH III profile, and Shuai Xue assisted us to plot the figure of the resistivity model. Walter Mooney and Stephanie Fovenyessy have helped to improve the original manuscript. The discussions at Coffice D3-422 of the SKLLE-IGGCAS inspired the interpretation. We acknowledge the authors of the SIMUL2000 algorithm for making this source code available (<http://www.geology.wisc.edu/~thurber/simul2000/>). All the figures in this paper were produced by using the Generic Mapping Tools (GMT) package (Wessel et al., 2013; Wessel & Smith, 1991). This research is supported by the Strategic Priority Research Program (B) of the Chinese Academy of Sciences (Grants XDB18000000 and XDB03010700) and the National Natural Science Foundation of China (Grants 41574056 and 41404051). Xiaofeng Liang is supported by the Youth Innovation Promotion Association, CAS (2017093). The waveform data recorded by the SANDWICH network can be accessed from SAL-IGGCAS (www.seislab.cn). All travel time data of Pg and Sg phases used in this study and the inverted Vp, Vp/Vs and Qp models derived in this study are provided as supporting information (Tables S4 to S7).

6. Conclusions

In this study, we collected earthquake data recorded by the SANDWICH and CNSN networks, as well as shot data obtained along the INDEPTH-III profile. We then applied the SIMUL2000 algorithm to invert these data for 3-D Vp and Vp/Vs models and simultaneously to relocate the local earthquakes with the updated velocity models. After the velocity inversion, we performed local attenuation tomography using t^* measurements from the relocated earthquakes. Finally, we presented and discussed our 3-D velocity (Vp and Vp/Vs ratio) and Qp models of the upper crust under the conjugate strike-slip fault zone in central Tibet. The low Vp anomalies near the surface generally correspond to the major sedimentary basins. A strong high Vp anomaly zone in the Tug Co basin probably reflects the raised Qiangtang anticline beneath the basin. The other near-surface high Vp anomalies are strongly related to the solidified sediments and metamorphic rocks in the study area. The relatively low Vp/Vs ratios indicate that quartz-rich rocks widely exist in the upper crust, in agreement with previous studies. From 0- to 10-km depth where we have good resolving ability, the study area is dominated by widespread low Vp anomalies around the BNS. These anomalies are also spatially correlated with the ophiolitic mélangé belt around the BNS. In view of, additionally, relatively heterogeneous Qp values from 0- to 10-km depth, our preferred explanation for the low Vp zone is that a sheared zone exists along a physically weak zone around the BNS in the upper crust of central Tibet. Due to the feasibility of a ductile or even partially molten middle/lower crust in central Tibet, the shear traction for the formation of the conjugate strike-slip faults comes from the flow of the middle/lower crust.

References

- Armijo, R., Tapponnier, P., Mercier, J. L., & Han, T. L. (1986). Quaternary extension in southern Tibet—Field observations and tectonic implications. *Journal of Geophysical Research*, 91(B14), 13,803–13,872. <https://doi.org/10.1029/JB091iB14p13803>
- Armijo, R., Tapponnier, P., & Tonglin, H. (1989). Late Cenozoic right-lateral strike-slip faulting in southern Tibet. *Journal of Geophysical Research*, 94(B3), 2787–2838. <https://doi.org/10.1029/JB094iB03p02787>
- Blisniuk, P. M., Hacker, B. R., Glodny, J., Ratschbacher, L., Bi, S. W., Wu, Z. H., et al. (2001). Normal faulting in central Tibet since at least 13.5 Myr ago. *Nature*, 412(6847), 628–632. <https://doi.org/10.1038/35088045>
- Bondar, I., Myers, S. C., Engdahl, E. R., & Bergman, E. A. (2004). Epicentre accuracy based on seismic network criteria. *Geophysical Journal International*, 156(3), 483–496. <https://doi.org/10.1111/j.1365-246X.2004.02070.x>
- Brune, J. N. (1970). Tectonic stress and the spectra of seismic shear waves from earthquakes. *Journal of Geophysical Research*, 75(26), 4997–5009. <https://doi.org/10.1029/JB075i026p04997>
- Chen, Q. Z., Freymueller, J. T., Wang, Q., Yang, Z. Q., Xu, C. J., & Liu, J. N. (2004). A deforming block model for the present-day tectonics of Tibet. *Journal of Geophysical Research*, 109, B01403. <https://doi.org/10.1029/2002JB002151>
- Chen, W. P., & Molnar, P. (1983). Focal depths of intracontinental and intraplate earthquakes and their implications for the thermal and mechanical properties of the lithosphere. *Journal of Geophysical Research*, 88(B5), 4183–4214. <https://doi.org/10.1029/JB088iB05p04183>
- Christensen, N. I. (1979). Compressional wave velocities in rocks at high-temperatures and pressures, critical thermal-gradients, and crustal low-velocity zones. *Journal of Geophysical Research*, 84(B12), 6849–6857. <https://doi.org/10.1029/JB084iB12p06849>
- Data Management Centre of China National Seismic Network. Waveform data of China National Seismic Network. Institute of Geophysics, China Earthquake Administration, 2007. doi:<https://doi.org/10.11998/SeisDmc/SN>, <http://www.seisdmc.ac.cn>.
- Ding, L., Kapp, P., & Wan, X. Q. (2005). Paleocene-Eocene record of ophiolite obduction and initial India-Asia collision, south central Tibet. *Tectonics*, 24, TC3001. <https://doi.org/10.1029/2004TC001729>
- Eberhart-Phillips, D. (1993). Local earthquake tomography: Velocities and Vp/vs-theory. In H. M. Iyer, & K. Hirahara (Eds.), *Seismic tomography: Theory and practice* (pp. 613–643). London, UK: Chapman and Hall.
- Eberhart-Phillips, D., & Chadwick, M. (2002). Three-dimensional attenuation model of the shallow Hikurangi subduction zone in the Raukumara Peninsula, New Zealand. *Journal of Geophysical Research*, 107(B2), 2033. <https://doi.org/10.1029/2000JB000046>
- England, P., & McKenzie, D. (1982). A thin viscous sheet model for continental deformation. *Geophysical Journal of the Royal Astronomical Society*, 70(2), 295–321. <https://doi.org/10.1111/j.1365-246X.1982.tb04969.x>

- England, P., & Molnar, P. (1997). Active deformation of Asia: From kinematics to dynamics. *Science*, 278(5338), 647–650. <https://doi.org/10.1126/science.278.5338.647>
- Evans, J., Eberhart-Phillips, D., and Thurber, C. H. (1994). User's manual for SIMULPS12 for imaging Vp and Vp/vs: A derivative of the 'Thurber' tomographic inversion SIMUL3 for local earthquakes and explosions, Open-File Report, 4–8.
- Gan, W. J., Zhang, P. Z., Shen, Z. K., Niu, Z. J., Wang, M., Wan, Y. G., et al. (2007). Present-day crustal motion within the Tibetan Plateau inferred from GPS measurements. *Journal of Geophysical Research*, 112, B08416. <https://doi.org/10.1029/2005JB004120>
- Gao, R., Chen, C., Lu, Z. W., Brown, L. D., Xiong, X. S., Li, W. H., & Deng, G. (2013). New constraints on crustal structure and Moho topography in Central Tibet revealed by SinoProbe deep seismic reflection profiling. *Tectonophysics*, 606, 160–170. <https://doi.org/10.1016/j.tecto.2013.08.006>
- Haines, S. S., Klemperer, S. L., Brown, L., Jingru, G. R., Mechie, J., Meissner, R., et al. (2003). INDEPTH III seismic data: From surface observations to deep crustal processes in Tibet. *Tectonics*, 22(1), 1001. <https://doi.org/10.1029/2001TC001305>
- He, J., Wang, J., Tan, F., Chen, M., Li, Z., Sun, T., et al. (2014). A comparative study between present and palaeo-heat flow in the Qiangtang Basin, northern Tibet, China. *Marine and Petroleum Geology*, 57, 345–358. <https://doi.org/10.1016/j.marpetgeo.2014.05.020>
- Huang, W. C., Ni, J. F., Tilmann, F., Nelson, D., Guo, J. R., Zhao, W. J., et al. (2000). Seismic polarization anisotropy beneath the central Tibetan Plateau. *Journal of Geophysical Research*, 105(B12), 27,979–27,989. <https://doi.org/10.1029/2000JB900339>
- Jiang, G., Gao, P., Rao, S., Zhang, L., Tang, X., Huang, F., et al. (2016). Compilation of heat flow data in the continental area of China (4th edition). *Chinese Journal of Geophysics-Chinese Edition*, 59(8), 2892–2910. <https://doi.org/10.6038/cjg20160815>
- Kapp, P., Taylor, M., Stockli, D., & Ding, L. (2008). Development of active low-angle normal fault systems during orogenic collapse: Insight from Tibet. *Geology*, 36(1), 7. <https://doi.org/10.1130/g24054a.1>
- Kapp, P., Yin, A., Harrison, T. M., & Ding, L. (2005). Cretaceous-Tertiary shortening, basin development, and volcanism in central Tibet. *Geological Society of America Bulletin*, 117(7), 865–878. <https://doi.org/10.1130/B25595.1>
- Klein, F. (2014). User's guide to HYPOINVERSE-2000, a Fortran program to solve for earthquake locations and magnitudes, version 1.40, June 2014, 9–25. <https://doi.org/10.13140/2.1.4859.3602>
- Klemperer, S. L. (2006). Crustal flow in Tibet: Geophysical evidence for the physical state of Tibetan lithosphere, and inferred patterns of active flow. *Geological Society, London Special Publications*, 268(1), 39–70. <https://doi.org/10.1144/GSL.SP.2006.268.01.03>
- Langin, W. R., Brown, L. D., & Sandvol, E. A. (2003). Seismicity of central Tibet from project INDEPTH III seismic recordings. *Bulletin of the Seismological Society of America*, 93(5), 2146–2159. <https://doi.org/10.1785/0120030004>
- Laske, G., Masters, G., Ma, Z., & Pasyanos, M. (2013). Update on CRUST1.0 - a 1-degree global model of Earth's crust. In *Geophysical research abstracts* (Vol. 15, Abstract EGU2013–2658). Vienna, Austria: EGU General Assembly.
- Li, Y., Wang, C., Dai, J., Xu, G., Hou, Y., & Li, X. (2015). Propagation of the deformation and growth of the Tibetan-Himalayan orogen: A review. *Earth-Science Reviews*, 143, 36–61. <https://doi.org/10.1016/j.earscirev.2015.01.001>
- Liang, S. M., Gan, W. J., Shen, C. Z., Xiao, G. R., Liu, J., Chen, W. T., et al. (2013). Three-dimensional velocity field of present-day crustal motion of the Tibetan Plateau derived from GPS measurements. *Journal of Geophysical Research: Solid Earth*, 118, 5722–5732. <https://doi.org/10.1002/2013JB010503>
- Liang, X. F., Chen, Y., Tian, X. B., Chen, Y. J., Ni, J., Gallegos, A., et al. (2016). 3D imaging of subducting and fragmenting Indian continental lithosphere beneath southern and central Tibet using body-wave finite-frequency tomography. *Earth and Planetary Science Letters*, 443, 162–175. <https://doi.org/10.1016/j.epsl.2016.03.029>
- Liang, X. F., Sandvol, E., Kay, S., Heit, B., Yuan, X. H., Mulcahy, P., et al. (2014). Delamination of southern Puna lithosphere revealed by body wave attenuation tomography. *Journal of Geophysical Research: Solid Earth*, 119, 549–566. <https://doi.org/10.1002/2013JB010309>
- Liang, X. F., Tian, X. B., Zhu, G. H., Wu, C. L., Duan, Y. H., Li, W., et al. (2016). SANDWICH: A 2D broadband seismic array in central Tibet. *Seismological Research Letters*, 87(4), 864–873. <https://doi.org/10.1785/0220150243>
- Lin, G., Shearer, P. M., Matoza, R. S., Okubo, P. G., & Amelung, F. (2014). Three-dimensional seismic velocity structure of Mauna Loa and Kilauea volcanoes in Hawaii from local seismic tomography. *Journal of Geophysical Research: Solid Earth*, 119, 4377–4392. <https://doi.org/10.1002/2013JB010820>
- Lin, G. Q. (2014). Three-dimensional compressional wave attenuation tomography for the crust and uppermost mantle of Northern and Central California. *Journal of Geophysical Research: Solid Earth*, 119, 3462–3477. <https://doi.org/10.1002/2013JB010621>
- Lu, Z., Gao, R., Li, Y., Xue, A., Li, Q., Wang, H., et al. (2013). The upper crustal structure of the Qiangtang Basin revealed by seismic reflection data. *Tectonophysics*, 606, 171–177. <https://doi.org/10.1016/j.tecto.2013.07.019>
- Maheo, G., Leloup, P., Valli, F., Lacassin, R., Arnaud, N., Paquette, J., et al. (2007). Post 4 Ma initiation of normal faulting in southern Tibet. Constraints from the Kung Co half graben. *Earth and Planetary Science Letters*, 256(1–2), 233–243. <https://doi.org/10.1016/j.epsl.2007.01.029>
- Mechie, J., Sobolev, S. V., Ratschbacher, L., Babeyko, A. Y., Bock, G., Jones, A. G., et al. (2004). Precise temperature estimation in the Tibetan crust from seismic detection of the alpha-beta quartz transition. *Geology*, 32(7), 601–604. <https://doi.org/10.1130/g20367.1>
- Meissner, R., Tilmann, F., & Haines, S. (2004). About the lithospheric structure of central Tibet, based on seismic: Data from the INDEPTH III profile. *Tectonophysics*, 380(1–2), 1–25. <https://doi.org/10.1016/j.tecto.2003.11.007>
- Min, Z., & Wu, F. T. (1987). Nature of the upper crust beneath central Tibet. *Earth and Planetary Science Letters*, 84(2–3), 204–210. [https://doi.org/10.1016/0012-821X\(87\)90086-0](https://doi.org/10.1016/0012-821X(87)90086-0)
- Mitchell, B. J. (1995). Anelastic structure and evolution of the continental crust and upper mantle from seismic surface wave attenuation. *Reviews of Geophysics*, 33(4), 441–462. <https://doi.org/10.1029/95RG02074>
- Molnar, P., & Lyoncaent, H. (1989). Fault plane solutions of earthquakes and active tectonics of the Tibetan Plateau and its margins. *Geophysical Journal International*, 99(1), 123–154. <https://doi.org/10.1111/j.1365-246X.1989.tb02020.x>
- Murphy, M. A., Saylor, J. E., & Ding, L. (2009). Late Miocene topographic inversion in southwest Tibet based on integrated paleoelevation reconstructions and structural history. *Earth and Planetary Science Letters*, 282(1–4), 1–9. <https://doi.org/10.1016/j.epsl.2009.01.006>
- Myers, S. C., Simmons, N. A., Johannesson, G., & Matzel, E. (2015). Improved regional and teleseismic P-wave travel-time prediction and event location using a global 3D velocity model. *Bulletin of the Seismological Society of America*, 105(3), 1642–1660. <https://doi.org/10.1785/0120140272>
- Peltzer, G., & Saucier, F. (1996). Present-day kinematics of Asia derived from geologic fault rates. *Journal of Geophysical Research*, 101(B12), 27,943–27,956. <https://doi.org/10.1029/96JB02698>
- Prieto, G. A., Parker, R. L., & Vernon, F. L. III (2009). A Fortran 90 library for multitaper spectrum analysis. *Computers & Geosciences*, 35(8), 1701–1710. <https://doi.org/10.1016/j.cageo.2008.06.007>
- Rapine, R., Tilmann, F., West, M., Ni, J., & Rodgers, A. (2003). Crustal structure of northern and southern Tibet from surface wave dispersion analysis. *Journal of Geophysical Research*, 108(B2), 2120. <https://doi.org/10.1029/2001JB000445>

- Rietbrock, A. (1996). *Entwicklung eines programmsystems zure konsistenten Auswertung grober seismologischer datensatze mit Anwendung auf die Untersuchung der absorptions-struktur der Loma-Prieta-region Kalifornien (development of an interactive analysis system for large seismological data sets; application to the determination of the absorption structure in the Loma Prieta region, California)*, Ph.D. dissertation. Munich, Germany: Ludwig-Maximilians-Universitat Munchen. 143
- Rietbrock, A. (2001). P wave attenuation structure in the fault area of the 1995 Kobe earthquake. *Journal of Geophysical Research*, *106*(B3), 4141–4154. <https://doi.org/10.1029/2000JB900234>
- Rothery, D. A., & Drury, S. A. (1984). The neotectonics of the Tibetan Plateau. *Tectonics*, *3*(1), 19–26. <https://doi.org/10.1029/TC003i001p00019>
- Royden, L. H., Burchfiel, B. C., & van der Hilst, R. D. (2008). The geological evolution of the Tibetan Plateau. *Science*, *321*(5892), 1054–1058. <https://doi.org/10.1126/science.1155371>
- Ryder, I., Wang, H., Bie, L., & Rietbrock, A. (2014). Geodetic imaging of late postseismic lower crustal flow in Tibet. *Earth and Planetary Science Letters*, *404*, 136–143. <https://doi.org/10.1016/j.epsl.2014.07.026>
- Ryerson, F. J., Tapponnier, P., Finkel, R. C., Meriaux, A., Der Woerd, J. V., Lasserre, C., et al. (2007). Applications of morphochronology to the active tectonics of Tibet. *Special Paper of the Geological Society of America*, *415*, 61–86. [https://doi.org/10.1130/2006.2415\(05\)](https://doi.org/10.1130/2006.2415(05))
- Sapin, M., Wang, X. J., Hirn, A., & Xu, Z. X. (1985). A seismic sounding in the crust of the Lhasa block, Tibet. *Annales Geophysicae*, *3*(5), 637–646.
- Scherbaum, F. (1990). Combined inversion for the three-dimensional Q structure and source parameters using microearthquake spectra. *Journal of Geophysical Research*, *95*(B8), 12,423–12,438. <https://doi.org/10.1029/JB095iB08p12423>
- Shearer, P. M. (2009). *Introduction to seismology*, (pp. 117–127). Cambridge, UK: Cambridge University Press.
- Shi, D., Zhao, W. J., Brown, L., Nelson, D., Zhao, X., Kind, R., et al. (2004). Detection of southward intracontinental subduction of Tibetan lithosphere along the Bangong-Nujiang suture by P-to-S converted waves. *Geology*, *32*(3), 209–212. <https://doi.org/10.1130/G19814.1>
- Singh, C., Shekar, M., Singh, A., & Chadha, R. K. (2012). Seismic attenuation characteristics along the Hi-CLIMB profile in Tibet from Lg Q inversion. *Bulletin of the Seismological Society of America*, *102*(2), 783–789. <https://doi.org/10.1785/0120110145>
- Solon, K. D., Jones, A. G., Nelson, K. D., Unsworth, M. J., Kidd, W. F., Wei, W., et al. (2005). Structure of the crust in the vicinity of the Bangong-Nujiang suture in central Tibet from INDEPTH magnetotelluric data. *Journal of Geophysical Research*, *110*, B10102. <https://doi.org/10.1029/2003JB002405>
- Styron, R., Taylor, M., & Okoronkwo, K. (2010). Database of active structures from the Indo-Asian collision. *Eos Transactions American Geophysical Union*, *91*(20), 181–182. <https://doi.org/10.1029/2010EO200001>
- Tapponnier, P., Peltzer, G., Dain, A. Y. L., Armijo, R., & Cobbold, P. (1982). Propagating extrusion tectonics in Asia: New insights from simple experiments with plasticine. *Geology*, *10*(12), 611–616. [https://doi.org/10.1130/0091-7613\(1982\)10<611:PETIAN>2.0.CO;2](https://doi.org/10.1130/0091-7613(1982)10<611:PETIAN>2.0.CO;2)
- Taylor, M., & Peltzer, G. (2006). Current slip rates on conjugate strike-slip faults in central Tibet using synthetic aperture radar interferometry. *Journal of Geophysical Research*, *111*, B12402. <https://doi.org/10.1029/2005JB004014>
- Taylor, M., & Yin, A. (2009). Active structures of the Himalayan-Tibetan orogen and their relationships to earthquake distribution, contemporary strain field, and Cenozoic volcanism. *Geosphere*, *5*(3), 199–214. <https://doi.org/10.1130/Ges00217.1>
- Taylor, M., Yin, A., Ryerson, F. J., Kapp, P., & Ding, L. (2003). Conjugate strike-slip faulting along the Bangong-Nujiang suture zone accommodates coeval east-west extension and north-south shortening in the interior of the Tibetan Plateau. *Tectonics*, *22*(4), 1044. <https://doi.org/10.1029/2002TC001361>
- Thatcher, W. (2007). Microplate model for the present-day deformation of Tibet. *Journal of Geophysical Research*, *112*, B01401. <https://doi.org/10.1029/2005JB004244>
- Thurber, C., & Eberhart-Phillips, D. (1999). Local earthquake tomography with flexible gridding. *Computers & Geosciences*, *25*(7), 809–818. [https://doi.org/10.1016/S0098-3004\(99\)00007-2](https://doi.org/10.1016/S0098-3004(99)00007-2)
- Thurber, C. H. (1983). Earthquake locations and three-dimensional crustal structure in the Coyote Lake area, Central California. *Journal of Geophysical Research*, *88*(B10), 8226–8236. <https://doi.org/10.1029/JB088iB10p08226>
- Thurber, C. H. (1993). Local earthquake tomography: Velocities and Vp/Vs-theory. In H. M. Iyer, & K. Hirahara (Eds.), *Seismic tomography: Theory and practice* (pp. 563–583). London, UK: Chapman and Hall.
- Tian, X. B., Wu, Q. J., Zhang, Z. J., Teng, J. W., & Zeng, R. S. (2005). Joint imaging by teleseismic converted and multiple waves and its application in the INDEPTH-III passive seismic array. *Geophysical Research Letters*, *32*, L08301. <https://doi.org/10.1029/2004GL021885>
- Wang, J. Y., & Huang, S. P. (1990). Compilation of heat flow data in the China continental area (2nd edition). *Seismology and Geology*, *12*(4), 361–364.
- Wang, L. Q., Pan, G. T., Ding, J., & Yao, D. S. (2013). *Guidebook of 1:1,500,000 geological map of the Qinghai-Xizang (Tibet) Plateau and adjacent areas* (pp. 1–288). Beijing, China: Geological Publishing House.
- Wang, Q., Wyman, D. A., Li, Z.-X., Sun, W., Chung, S.-L., Vasconcelos, P. M., et al. (2010). Eocene north-south trending dikes in central Tibet: New constraints on the timing of east–west extension with implications for early plateau uplift? *Earth and Planetary Science Letters*, *298*(1–2), 205–216. <https://doi.org/10.1016/j.epsl.2010.07.046>
- Wang, Q., Zhang, P. Z., Freymueller, J. T., Bilham, R., Larson, K. M., Lai, X., et al. (2001). Present-day crustal deformation in China constrained by global positioning system measurements. *Science*, *294*(5542), 574–577. <https://doi.org/10.1126/science.1063647>
- Wei, S., Chen, Y. J., Sandvol, E., Zhou, S., Yue, H., Jin, G., et al. (2010). Regional earthquakes in northern Tibetan Plateau: Implications for lithospheric strength in Tibet. *Geophysical Research Letters*, *37*, L19307. <https://doi.org/10.1029/2010GL044800>
- Wei, W. B., Unsworth, M., Jones, A., Booker, J., Tan, H. D., Nelson, D., et al. (2001). Detection of widespread fluids in the Tibetan crust by magnetotelluric studies. *Science*, *292*(5517), 716–719. <https://doi.org/10.1126/science.1010580>
- Wessel, P., & Smith, W. H. F. (1991). Free software helps map and display data. *Eos, Transactions American Geophysical Union*, *72*(41), 441–446. <https://doi.org/10.1029/90EO00319>
- Wessel, P., Smith, W. H. F., Scharroo, R., & Wobbe, J. L. A. (2013). Generic mapping tools: Improved version released. *Eos, Transactions American Geophysical Union*, *94*(45), 409–410. <https://doi.org/10.1002/2013EO450001>
- Williams, H., Turner, S., Kelley, S., & Harris, N. (2001). Age and composition of dikes in southern Tibet: New constraints on the timing of east-west extension and its relationship to postcollisional volcanism. *Geology*, *29*(4), 339–342. [https://doi.org/10.1130/0091-7613\(2001\)029<0339:aacodi>2.0.co;2](https://doi.org/10.1130/0091-7613(2001)029<0339:aacodi>2.0.co;2)
- Xie, J., Gok, R., Ni, J., & Aoki, Y. (2004). Lateral variations of crustal seismic attenuation along the INDEPTH profiles in Tibet from Lg Q inversion. *Journal of Geophysical Research*, *109*, B10308. <https://doi.org/10.1029/2004JB002988>
- Yin, A., & Harrison, T. M. (2000). Geologic evolution of the Himalayan-Tibetan orogen. *Annual Review of Earth and Planetary Sciences*, *28*(1), 211–280. <https://doi.org/10.1146/annurev.earth.28.1.211>

- Yin, A., & Taylor, M. H. (2011). Mechanics of V-shaped conjugate strike-slip faults and the corresponding continuum mode of continental deformation. *Geological Society of America Bulletin*, 123(9–10), 1798–1821. <https://doi.org/10.1130/B30159.1>
- Zhang, K., Wang, G., Ji, J., Luo, M., Kou, X., Wang, Y., et al. (2010). Paleogene-Neogene stratigraphic realm and sedimentary sequence of the Qinghai-Tibet Plateau and their response to uplift of the plateau. *Science China-Earth Sciences*, 53(9), 1271–1294. <https://doi.org/10.1007/s11430-010-4048-2>
- Zhang, P. Z., Shen, Z., Wang, M., Gan, W. J., Burgmann, R., & Molnar, P. (2004). Continuous deformation of the Tibetan Plateau from global positioning system data. *Geology*, 32(9), 809–812. <https://doi.org/10.1130/G20554.1>
- Zhang, X., Brown, D., & Deng, Y. (2011). Crustal composition model across the Bangong-Nujiang suture belt derived from INDEPTH III velocity data. *Journal of Geophysics and Engineering*, 8(4), 549–559. <https://doi.org/10.1088/1742-2132/8/4/007>
- Zhang, Z. J., & Klempner, S. L. (2005). West-east variation in crustal thickness in northern Lhasa block, central Tibet, from deep seismic sounding data. *Journal of Geophysical Research*, 110, B09403. <https://doi.org/10.1029/2004JB003139>
- Zhao, J., Yuan, X., Liu, H., Kumar, P., Pei, S., Kind, R., et al. (2010). The boundary between the Indian and Asian tectonic plates below Tibet. *Proceedings of the National Academy of Sciences current issue*, 107(25), 11,229–11,233. <https://doi.org/10.1073/pnas.1001921107>
- Zhao, L. F., Xie, X. B., He, J. K., Tian, X. B., & Yao, Z. X. (2013). Crustal flow pattern beneath the Tibetan Plateau constrained by regional Lg-wave Q tomography. *Earth and Planetary Science Letters*, 383, 113–122. <https://doi.org/10.1016/j.epsl.2013.09.038>
- Zhao, W., Mechie, J., Brown, L. D., Guo, J., Haines, S., Hearn, T., et al. (2001). Crustal structure of central Tibet as derived from project INDEPTH wide-angle seismic data. *Geophysical Journal International*, 145(2), 486–498. <https://doi.org/10.1046/j.0956-540x.2001.01402.x>
- Zheng, X. F., Yao, Z. X., Liang, J. H., & Zheng, J. (2010). The role played and opportunities provided by IGP DMC of China National Seismic Network in Wenchuan earthquake disaster relief and researches. *Bulletin of the Seismological Society of America*, 100(5b), 2866–2872. <https://doi.org/10.1785/0120090257>
- Zhu, D. C., Li, S. M., Cawood, P. A., Wang, Q., Zhao, Z. D., Liu, S. A., & Wang, L. Q. (2016). Assembly of the Lhasa and Qiangtang terranes in central Tibet by divergent double subduction. *Lithos*, 245, 7–17. <https://doi.org/10.1016/j.lithos.2015.06.023>
- Zhu, G., Liang, X., Tian, X., Yang, H., Wu, C., Duan, Y., et al. (2017). Analysis of the seismicity in Central Tibet based on the SANDWICH network and its tectonic implications. *Tectonophysics*, 702, 1–7. <https://doi.org/10.1016/j.tecto.2017.02.020>